

MIT Open Access Articles

Volta potential mapping of the gradient strengthened layer in 20CrMnTi by using SKPFM

The MIT Faculty has made this article openly available. **Please share** how this access benefits you. Your story matters.

As Published: <https://doi.org/10.1007/s10853-020-04815-z>

Publisher: Springer US

Persistent URL: <https://hdl.handle.net/1721.1/131864>

Version: Author's final manuscript: final author's manuscript post peer review, without publisher's formatting or copy editing

Terms of Use: Article is made available in accordance with the publisher's policy and may be subject to US copyright law. Please refer to the publisher's site for terms of use.



Volta potential mapping of the gradient strengthened layer in 20CrMnTi by using SKPFM

Cite this article as: Tao Cheng, Wei Shi, Song Xiang and Ronald G. Ballinger, Volta potential mapping of the gradient strengthened layer in 20CrMnTi by using SKPFM, Journal of Materials Science <https://doi.org/10.1007/s10853-020-04815-z>

This Author Accepted Manuscript is a PDF file of an unedited peer-reviewed manuscript that has been accepted for publication but has not been copyedited or corrected. The official version of record that is published in the journal is kept up to date and so may therefore differ from this version.

Terms of use and reuse: academic research for non-commercial purposes, see here for full terms. <https://www.springer.com/aam-terms-v1>

Author accepted manuscript

Volta potential mapping of the gradient strengthened layer in 20CrMnTi by using SKPFM

Tao Cheng^a, Wei Shi^{a,b,*}, Song Xiang^{a,b,c,*}, Ronald G. Ballinger^c

a College of Materials and Metallurgy, Guizhou University, Guiyang 550025, China

b Key Laboratory for Mechanical Behavior and Microstructure of Materials of Guizhou Province, Guizhou University, Guiyang 550025, China

c H.H. Uhlig Corrosion Laboratory, Massachusetts Institute of Technology, Cambridge, MA 02139, United States

The e-mail addresses and ORCID

Tao Cheng- 1224280372@qq.com

Wei Shi- wshi@gzu.edu.cn ORCID- 0000-0002-5427-5216

Song Xiang- sxiang@gzu.edu.cn

Ronald G. Ballinger- hvymet@mit.edu

Abstract: The purpose of this paper is to use SKPFM to characterize the gradient strengthened layer induced by the ultrasonic surface rolling process (USRP). A correlation between the dislocation, residual stresses, and SKPFM derived Volta potential was obtained using Scanning Kelvin probe force microscopy (SKPFM),

* Corresponding authors:

E-mail addresses: wshi@gzu.edu.cn (Wei Shi), sxiang@gzu.edu.cn (Song Xiang)

electron back-scattered diffraction (EBSD), transmission electron microscopy (TEM) and X-ray stress analysis. In the plastic deformation region, a localized fluctuation of Volta potential at structural interface was formed due to the decreased electron work function caused by dislocations pile-up, where the Volta potential at the interface is higher than the surrounding region. However, in the elastic deformation region, due to the slight influence of residual tensile stress, the potential value is still higher than the unreformed zone but much lower than the plastic deformation region, and the Volta potential map tended to be flat without localized potential fluctuations.

Keywords: SKPFM; Ultrasonic surface rolling processing; Volta potential; Residual stress gradient;

1 Introduction

Ultrasonic surface rolling process (USRP) is an effective strategy to reduce the surface roughness of alloy steel, introduce residual compressive stress in the surface layer, and improve the wear resistance and fatigue resistance [1, 2]. Since severe plastic deformation significantly alters the microstructure of the surface, a great deal of research has been done on the effect of ultrasonic treatment on corrosion properties [3-11]. In most cases, mechanical deformation that leads to grain refinement usually results in a decrease in average corrosion resistance due to large amount of grain boundary, except for other related improvements such as passivation, roughness, pitting resistance, etc. But, in the strengthened layer, there are two types of main gradient changes, the grain size gradient and the residual stress gradient, although the correlation of grain size with

corrosion behaviour was well known, how the residual stress field affecting the electrochemical activity was not clear. Chui et al. [12] investigated the effect of surface nanocrystallization induced by fast multiple rotation rolling (FMRR) on corrosion behavior of 316L stainless steel, and the results showed that the FMRR treated 316L stainless steel with a surface nanocrystallized layer reduced the corrosion resistance in a 3.5% NaCl solution and enhanced the pitting corrosion rate in a FeCl₃ solution. Sun et al. [8] studied the localized corrosion behaviour of 7150 aluminum alloy after ultrasonic shot peening (USSP) and found that the USSP enhanced the pit initiation resistance but accelerated the pit propagation kinetics of 7150 aluminum alloy due to the constricted pit morphology caused by a gradient microstructure. Lu et al. [11] have shown that nanocrystalline boundaries of AISI 316L stainless steel by surface mechanical attrition treatment (SMAT) reduced the corrosion resistance, whereas twin boundaries improved the corrosion resistance in 0.05 M H₂SO₄ + 0.25 M Na₂SO₄.

SKPFM measures the Volta potential with nanometer resolution and an energy sensitivity better than 0.1 eV [13]. By reducing the size of the Kelvin probe to the nanoscale and combining it with atomic force microscope (AFM) [14], the resulting SKPFM can produce simultaneous maps of the surface topography and the corresponding Volta potential in local scale to gain insight into the local electrochemical nobility of heterogeneous microstructures [15]. Örneke et al. [16] conducted the SKPFM study on the difference between the γ and δ phases of duplex stainless steel, suggesting that regions with higher contact potential differences tended to preferentially corrode. E.

Rahimi et al.[17] revealed that the Cu region has a higher Volta potential than the Ti region, and corrosion mainly occurred on the Cu side due to the increasing growth of the Ti passive film. Ma et al [18] studied the work function (WF) variation on different grain orientations of 90Cu-10Ni alloy by using SKPFM and found that grains close to (100) exhibited lower WF with lower dissolution rate, whereas grains close to (111) with higher WF dissolved faster. As mentioned above, the effect of residual stress gradient on the localised corrosion in the strengthen layer was not clearly known, hence, whether SKPFM technique can be used as a method to reveal the correlation of residual stress gradient with Volta potential has aroused great interest.

As a matter of fact, Volta potential is a material specific property which is highly sensitive to different elements in alloys, thus, the SKPFM was widely used in the researches of alloy or multiphase structure, but concerning about the effect of residual stress filed on the Volta potential measured by SKPFM, there was lack of publications. Theoretically, the feasibility can be found in studies using scanning Kelvin probe (SKP), because the principle of the two technique is basically the same. Although the measured Volta potential is highly sensitive to the environment and the surface condition of the tested material, the electron work function (EWF) difference between the tip and the metal establish the Volta potential difference [19]. Li et al. [20] studied the EWF changes of copper under various loading condition by SKP, found that in the elastic deformation range, the tensile strain decreased the EWF and vice versa, while in the plastic deformation range, the EWF always decreased with plastic strain no matter it was

tensile or compressive. Furthermore, Li et al. [21] also demonstrated that the EWF at grain boundaries was decreased owing to the lattice distortion or defects such as dislocation, in contrast to the grain interior. However, the effective spatial resolution of the SKP is limited. The sampling region for the potential measured from the metal surface is limited to the submillimeter-scale [20, 22]. Thus, the SKPFM is an improved way to characterize the gradient structure for its extremely higher spatial resolution.

In this work, SKPFM was used to characterize the cross section of 20CrMnTi gradient layer in combination with grain refinement and dislocation density characterized by EBSD and TEM. The 20CrMnTi steel is a commercial low carbon steel for gear manufacturing and the microstructures of the quenched 20CrMnTi are mainly martensite and retained austenite. After the high-frequency cold deformation by USRP, a gradient changed strengthening layer with thickness of 100-300 μm is formed. Hence, the strengthened layer of 20CrMnTi is an ideal gradient layer with residual stress, grain size refinement and minor element changes. It will be shown that the correlation of the dislocation density, residual stress with the SKPFM measured Volta potential in the 20CrMnTi steel gradient layer caused by USRP.

2 Materials and methods

2.1 Materials

The 20CrMnTi steel rods with a chemical composition of (in wt.%) Cr: 1.2; Mn: 1.0, Ti: 0.08; C: 0.2; Si: 0.3; Ni: 0.03; Cu: 0.03 ; Fe: balance; were used as substrate

materials. To obtain a martensite microstructure, the raw material was heat treated at 870°C for 1 h, quenched in a cold saline solution, tempered at 200°C for 2h and cooled in air. The tempered specimens were cut into round bars with a diameter of 10 mm and a length of 100 mm, and then ground using 320#, 600#, 1200#, 2000# sand paper.

2.2 USRP

The ultrasonic surface rolling treatment of 20CrMnTi steel was carried out on the ultrasonic rolling lathe (CAG150, China). Three types of samples with gradient deformation layers were obtained by adjusting the working pressure of the ultrasonic rolling head to 0.1, 0.15 and 0.2 MPa, which was the variable that controlled the production of the strengthened surface layer on the specimen. After the specimens were removed from the ultrasonic rolling lathe, the surface lubricating oil that was used to reduce the roughness of the sample in the ultrasonic rolling machine was immediately removed using acetone, and the samples were dried using cold air. Cross-section cut from the processed region is shown in Fig.1, where Z axis was the observation direction perpendicular to the cross section, X axis was the deformation direction tangent to the arc and the Y axis was the direction toward the center. Then, cross-section was polished with argon ions and then characterized by SEM, SKPFM and EBSD. In addition, cross sections were subjected to electrochemical test and residual stress test, the latter was stripped by electrolytic polishing. A diagram of the overall experimental approach is shown in Fig. 1, and the experimental procedures are described in detail in the following subsections.

2.3 Electrochemical method

The processed specimens were used as working electrodes. A heat-shrinkable tube was used to wrap the unprocessed region, and silicone rubber was used to seal the gap between the heat-shrinkable tube and the specimen. The exposed region of the working electrode was 0.5 cm^2 . Electrochemical testing was performed in a borate buffer solution (pH=8.45) with $0.05 \text{ mol.L}^{-1} \text{ Cl}^-$ contamination at $30 \text{ }^\circ\text{C} \pm 1 \text{ }^\circ\text{C}$ using a water bath. An electrochemical workstation (Model CS350, Corrtest, China) was used for the potentiodynamic polarization curves measurements. A saturated calomel electrode (SCE) and Pt plate electrode were used as the reference electrode and counter electrode, respectively. Potentiodynamic polarization curves were obtained at a scan rate of 0.5 mV.s^{-1} , ranging from -0.6 V vs. the OCP (open circuit potential) to $+0.8 \text{ V}$ vs. the OCP.

2.4 Residual stress measurements

The axial residual stress (normal stress) of the samples rolled under 0.1 MPa, 0.15 MPa and 0.2 MPa pressures was measured by layer stripping method (electrolytic polishing) on the GNR type X-ray diffractometer using fixed bits of heeling and the $\sin^2\psi$ method with ψ angles of 0° , $\pm 10^\circ$, $\pm 20^\circ$, $\pm 30^\circ$, and $\pm 40^\circ$. The XRD was conducted with $\text{r-K}\alpha$ radiation, a test collimator tube diameter of 2 mm, the {211} peak, a 20 kV tube voltage, a tube current of 5 mA, a $147^\circ \sim 167^\circ$ scan range, and a step distance of 0.1° . Combined with the characteristics of the open testing platform of GNR residual stress diffractometer, the electrolytic polishing of samples can be carried out on the residual stress diffractometer working table to achieve in-situ layer stripping. The test points at

different depths do not change in the X and Y directions in the coordinate system of the work table, and the change in the height (normal) direction is exactly the strip depth.

Therefore, the test regions for the X-ray residual stress measurement before and after stripping were consistent. By in-situ layer stripping of the sample on the X-ray diffractometer, the in-depth residual stress distributions were obtained.

2.5 SKPFM measurement

2.5.1 Sample Preparation

To minimize the effects of the roughness, metal passivation and adsorption on the variability of the acquired Volta potential values, samples were prepared using the same steps for each map acquisition. To create a fresh and smooth surface for the SKPFM measurements, the samples were all polished with argon ions after mechanical polishing, because argon ion polishing can remove a damaged layer and reveal the internal structure of a crystal, especially the grain boundaries, and the roughness can be reduced to the nanometer level. Following each polishing step, samples were sequentially rinsed with deionized water and nondenatured absolute alcohol and then dried with compressed air. Following polishing and immediately prior to SKPFM imaging, the sample was cleaned by ultrasonication in ethanol and then dried with compressed ultrahigh purity (UHP) nitrogen gas.

2.5.2 Testing parameters

A MultiMode 8 atomic force microscope from Veeco Instruments (AFM) with a

Nanoscope V8.15 acquisition program from Bruker was used. The working principles and technical details of SKPFM have been described in other literature reports [23-26]. A standard MESP probe with n-type antimony doped-silicon coated with magnetic CoCr on the front and back sides of the probe was used. The SKPFM was carried out by employing the dual-scan mode, with the first scan determining the surface topography, followed by a second scan in which the probe was lifted up to 80 nm to obtain the Volta potential data. The SKPFM measurements were carried out in ambient air at room temperature with 30% relative humidity, a pixel resolution of 256×256 , and a scan frequency rate of 0.996 Hz. The SKPFM data analysis was performed with NanoScope Analysis 1.5 software. According to the working principle of SKPFM, the equation for the Volta potential difference between the specimen and tip (with bias) is as shown below: [19]

$$V_{\text{CPD}} = \Psi_{\text{T}} - \Psi_{\text{S}}$$

where Ψ_{S} is the Volta potential of the sample, Ψ_{T} is the Volta potential of the tip (MESP probe), and V_{CPD} is the measured Volta potential difference. The reliability of the tip used was assessed by measuring the Volta potential of a standard gold sample, and maximum potential differences of 1–3 mV were measured prior to and after the test during the same measurement day with no significant variation, indicating good tip quality and a maximum sensitivity of the system [24]. Örnek et al. [19] suggested that a polarity convention for SKPFM-measured Volta potentials is needed to improve the interpretation. In this study, the Volta potential maps were not inverted, and a bias

voltage of 750mV was applied to the tip. Therefore, the measured Volta potential difference with positive values indicate lower work functions and, hence, lower Volta potentials of the sample relative to the tip, hence, it can be inferred that the sample is less noble (anodic) than the tip. Here, high Volta potential value (more positive) measured by the SKPFM indicate anodic (less noble) characters whereas low Volta potential value (less positive) indicate cathodic regions.

2.6 EBSD measurements

To demonstrate the effect of cold-rolling on microstructure development, three specimens that were rolled under different pressures (0.1 MPa, 0.15 MPa and 0.2 MPa) were polished with argon ions and characterized by EBSD. The microstructures of the gradient deformation layer were studied using an FEI Quanta 650 scanning electron microscope (SEM) operated at an acceleration voltage of 20 kV. Data acquisition and analysis were carried out with a Nordlys EBSD detector from Oxford Instruments equipped with Channel 5 software. The plastic deformation regions of specimens, which were within approximately 100 μm from the edge, were chosen for the EBSD analysis at a step size of 0.2 μm .

2.7 TEM measurements

The dislocation density of samples with different strains was measured by TEM. TEM analysis was conducted on an FEI TECNAI G2 F20 microscope with a Schottky thermal field emission gun at an accelerating voltage of 200 kV. TEM samples were

prepared by twin-jet electro-polishing in an alcohol solution of 10% HClO_4 at a temperature of 20 °C and Voltage of 40 V after the specimens were mechanically ground to a thickness of 50 μm to protect the rolled surface.

3 Results

3.1 Electrochemical behaviour

Polarization curves for the materials treated with different rolling pressures in the solution with $\text{pH}=8.45$ and $\text{Cl}^- = 0.05 \text{ mol/L}$ are shown in Fig. 2. The anodic passive range changed with the rolling pressure and decreased as the rolling pressure increased, as shown in Fig.2. The extracted data (the inset of Fig. 2) including corrosion current density and passivation range are presented in Fig. 3. The passive current density for the 0.2 MPa pressure is nearly twice that for the 0.1 MPa pressure, indicating a degradation of the corrosion resistance with increasing rolling pressure. Furthermore, the breakdown potential (E_b) exhibited a negative shift ($\sim 130 \text{ mV}$) when the rolling pressure exceeded 0.2 MPa. Moreover, the specimens treated with pressure 0.20 MPa exhibited prebreakdown of the passive film.

3.2 EBSD characterization

To assess the degree of the grain refinement, inverse pole figures are shown in Fig.

4. As shown, the grain size of the strengthened layer was reduced, due to the severe deformation and breaking up of grains after cold deformation. The statistical results of the grain size are shown in Fig. 5. The average grain size at a pressure of 0.1 MPa was

1.37 μm , while the grain size at a pressure of 0.2 MPa decreased to 1.19 μm , and the fraction of fine grains (average diameter less than 2 μm) increased as the static pressure was increased.

3.3 TEM characterization of the gradient structures

TEM micrographs of the treated and untreated samples are presented in Fig. 6. As expected, the lath martensite is formed during rapid cooling and have a substructure of dislocations, as shown for the untreated sample in Fig. 6a. The dislocation density is not high, as evidenced by the magnified image in the insert of Fig. 6a, which still reveals a small amount of residual austenite (Ar). For simplicity, its local density of $\sim 0.91 \times 10^{16} \text{ m}^{-2}$ is roughly determined by the Fourier-reconstructed image (Fig. 6b), although such density is larger than the real value because of the limited area measurement. USRP deformation results in dislocation multiplication, whereas homogeneous deformation does not occur at each lath at a lower stress level. For example, dislocations were pinned at lath boundaries and dislocation tangles have been developed into most of laths after 0.1 MPa treatment, leading to a dramatic increase in dislocation density ($\sim 1.55 \times 10^{16} \text{ m}^{-2}$). However, the low-density zone is still visible in some of laths, highlighted by white arrow in Fig. 6c. As the rolling pressure increased to 0.15 MPa, the relatively homogeneous deformation occurred, leading to further increase in density and gradual evolution into dislocation cells from tangles (Fig. 6e). A further increase in pressure results in severe deformation of the laths, evidenced by the significant accumulation of dislocations (Fig. 6g) with a density as high as $\sim 1.95 \times 10^{16} \text{ m}^{-2}$ (Fig. 6h). The statistical

results indicate that dislocation density increases dramatically with the increase of treated pressure, and subsequently tends to become steady at a certain pressure higher than 0.2 MPa (Fig. 7).

3.4 The surface morphology

Fig. 8 shows the surface morphology of the sample treated by USRP (0.2MPa) after argon ion polishing, where Figs. 8a (SEM) and c (AFM) are close to the sample edge (strengthened layer), while Fig. 8b (SEM) and d (AFM) are the centre region of the sample (matrix). Fig. 8a and c indicate that structures in the strengthened layer were all inclined towards the rolling direction and squeezing each other, leading to plastic flow. Plastic deformation amount decreases gradually along depth from the surface, which is similar to the tendency of low carbon steel after 60 min SMAT [19]. Therefore, no obvious plastic deformation was observed in the central region of the sample (Fig. 8b and d). The purpose of polishing with argon ions was to show the contrast image of microstructure. It can be seen that the polished surface was not flat but appeared surface relief, and the different height of topography was due to different the ion beam polishing resistant between grains or damaged microstructures. Although the surface looks uneven, the surface height fluctuation caused by argon ion impact is only 200nm. If the grain boundary is eroded by corrosion, the grain boundary corrosion depth may reach hundreds of nanometers, even micron level. Therefore, the release of stored energy can be avoided by argon ion polishing and by not using chemical etching.

3.5 SKPFM-Volta potential map

The topography and corresponding Volta potential maps for the 0.2 MPa condition at different depths from the surface are shown in Fig. 9. It can be seen that there was a certain relationship between the Volta potential and the morphology at a depth of 45 μm from the surface shown in Fig. 9a. The potential map shows positive values (the tip is biased), which means that the entire microstructure was less noble (anodic) than the AFM tip. The potential map at the recessed region displays a potential peak (a purple region confined by a white dotted line) that are higher than those of the surrounding region, and hence, a local Volta potential gradient was formed. However, it was found that the potential was not completely consistent with the surface height, when the white dotted frame line was transferred to the morphology.

Fig. 9b also displays the Volta potential peaks. Several local potential peaks occurred not only in the recessed regions but also in the protruding regions, indicating that these regions with steep potential changes had a high local corrosion activity. Given the distance tracking advantage of the SKPFM method, the effect of the surface roughness (height difference) on the Volta potential was not dominant. However, the distribution of the Volta potential near the matrix (Fig. 9c for a depth of 800 μm from the surface) was very stable and did not contain fluctuations, whereas the morphology exhibited the same characteristics (Figs. 9a and b), especially with regards to the roughness, which was basically consistent with Fig. 9a and was also 200 nm. Hence, the Volta potential distribution of the gradient layer was closely associated with other factors,

such as the residual stress gradient caused by USRP.

Fig. 10 shows the topography and corresponding Volta potential information at different depths from the surface of the material treated at 0.15 MPa. As an illustration, the potential peaks occurred only in the strengthened layer closest to the surface (Fig. 10a), which should also result in a microstructure that is more susceptible to corrosion (less noble) than the areas with a uniform potential distribution (Figs. 10 b and c). This phenomenon also appeared on the material treated at 0.1 MPa (Fig. 11), in which only the region closest to the surface had potential peaks, but the region 100 μm deep from the surface and near the matrix possessed a uniform potential distribution. Therefore, consistent with Fig. 9, the Volta potential distribution was closely related to the strengthened layer caused by ultrasonic surface rolling (Figs. 10 and 11).

To investigate the correlation between the residual stress and the Volta potential distribution, measurements of the Volta potential and residual stress along the gradient layer were conducted on each specimen. Fig. 12 displays the Volta potential and residual stress at different positions. The right ordinate axis presents the in-depth residual stress.

It can be seen that the variation of the residual stress in the gradient layer first increased and then decreased. The increase in the rolling pressure increased the depth of the affected layer. The depth of the residual stress layer in the material treated at 0.2 MPa increased to 900 μm (Fig. 12 c), whereas the depths of the residual stress layers were 600 μm and 700 μm for the materials treated at 0.1 MPa and 0.15 MPa, respectively (Figs. 12 a and b). The left ordinate axis presents the average Volta potential value and

Volta potential distribution (subplots) at different depths from the surface, where the average Volta potential is the average value of three different regions of the same depth, and one of the three regions constitutes the potential distribution (subplots). Previously, the distribution of the Volta potential in each sample at different depths from the surface was studied (Figs. 9, 10 and 11), which were close to the surface, approximately 100 μm away from the surface and close to the matrix.

As illustrated in Fig. 12, all potential curves showed a general trend. The average Volta potential decreased steeply in the first 300 μm , where the residual stress was large, varied more than 100 mV, then fluctuated smoothly with depth and eventually became stable. The variation of the Volta potential with the residual stress is consistent with the studies of the EWF under different degrees of deformation and yielding [20, 27]. The maximum average Volta potential occurred in the region with a relatively high residual stress, where the Volta potential increased by 130–200 mV compared to that of the matrix where no stress was applied. As the residual stress decreased sharply, the Volta potential smoothly decreased and eventually became stable when the residual stress approached zero. However, it is worth noting that the Volta potential values were different at the locations where residual stresses were the same (depths of approximately 300 μm and 0 μm from the surface). Hence, the rise in the potential near the surface may be due to other factors, such as dislocation accumulation at the grain boundaries and an increase in the dislocation density with an increase in the rolling pressure.

3.6 Morphology of the polished and etched cross-sections

To characterize the anodic activity at the grain boundaries, three specimens with polished surfaces were immersed in a picric acid etching solution for 2 min. The etched morphology is shown in Fig. 13. The width of the grain boundaries close to the surface was obviously larger than that far away from the surface. For example, in the material treated at 0.1 MPa, the width of the grain boundary closest to the surface reached 0.9 μm (Fig. 13 a), while the width away from the surface was only 0.22 μm (Fig. 13 d). This phenomenon was also observed in the materials treated at 0.15 MPa and 0.2 MPa. A comparison of the Volta potential curve (Fig. 12) to the corrosion morphology (Fig. 13), suggested that the anodic (less noble) character along the gradient layer was decreased as the average Volta potential values decreased. In addition, the surface of the material treated at 0.2 MPa had wider grain boundaries (reached to 1.5 μm) than those in the deformation layer, which is consistent with the high potential peak in Fig. 9, indicating local corrosion-activity. This behaviour was also associated with strain-induced dislocation; as the dislocation density increased, the grain boundary corrosion activity increased.

4 Discussion

The statistic results in Fig.12 clearly demonstrated a gradient change of Volta potential indeed existed in the strengthened layer. However, it is worth noting that the Volta potential values were different at the locations where residual stresses were the same (depths of approximately 300 μm and 0 μm from the surface). This result suggests

that the Volta potential may not always consistent with residual stress, thus, what factors in the gradient layer essentially induced the response of Volta potential need to be discussed. As stated above, the electron work function difference establish the Volta potential difference, and the decrease of the EWF can be considered as an increased tendency for electron transfer [19]. Li et.al [28] proposed a simple electrostatic action model to investigate the effect of a dislocation on the EWF of a one-dimensional lattice. In this model, the enlarged atomic spacing induced by dislocation-related strain fields leads to the potential well shallower and the electron binding force weaker, and hence a lowered work function. Thus, the atomic spacing and the dislocation density are the key factors account for the Volta potential change in the strengthened layer.

The schematic diagram as shown in Fig. 14 summarized the results presented in Fig.9-11, which clearly shown the correlation of Volta potential difference with the localized dislocation density. As generally known, the USRP generated a gradual decreased plastic deformation layer along the depth from the surface, the plastic deformation facilitates the dislocations pile-up near the grain boundary and the interface of martensitic lath. Thus, at the region near the surface, the localised high dislocation density caused by dislocations pile-up stimulate the Volta potential change, as demonstrated by the linear potential profiles marked by the red line in Fig. 9 a shown in Fig. 15. In the linear profiles, the potential line does not match the topography. The region of the high potential is wider than the interface, as shown in the shaded region. while at the region without plastic deformation, the more homogeneous distribution of

dislocation density result in the flattened Volta potential map. Hence, the gradually decreased Volta potential difference essentially revealed the reduction tendency of dislocation density at different depth.

However, the dislocation density could not be the only factor that determines the Volta potential in the strengthened layer. The plastic deformation region cannot cover the entire region caused by USRP according to the residual stress affection. From a mechanical equilibrium point of view, the intense plastic deformation near the surface generate the residual compress stress, while in the deeper region, a residual tensile stress must be generated for mechanical equilibrium as shown in Fig. 16, therefore, the gradient layer is divided into two regions along the depth, namely, A-B (plastic deformation) and B-C (elastic deformation). As stated above, in the plastic deformation, the Volta potential is mainly controlled by the dislocation density. But in the elastic deformation region, the dislocation density could not accumulate from the weakened tensile stress, thus, the residual stress is considered to be the main factor that controlled the following Volta potential in the B-C range.

Briefly, according to the principle of X-ray residual stress analyser, the principle is based on the famous Bragg equation, $2d\sin\theta = n\lambda$. By measuring the diffraction angle changes ($\Delta\theta$), the atomic plane spacing change (Δd) could be gained. According to Hooke's law and the modulus of elasticity, the residual stress of the material could be calculated. Presently, the stripping method is mostly used to obtain the internal residual

stress, when it is combined with XRD measurements, where milling and electrolysis are the two main methods [29]. When the layer with residual stress is stripped, the residual stress is redistributed and released [29, 30]. Therefore, there is a deviation between the measured residual stress and the theoretical residual stress, and the further away the sample surface, the greater the deviation [30]. According to this theory, the theoretical and measured residual stress curves are plotted in Fig. 16. The combination of electropolishing and XRD tests did not measure the tensile residual stress due to stress release (Fig. 16), but it is theoretically present. In another word, the tensile residual stress also enlarged the atomic spacing and corresponding reduction of Volta potential difference in the B-C range. Obviously, the change of Volta potential in the B-C range was significantly smaller than the change in the A-B range. This result indicated that the expansion degree of lattice plane spacing caused by residual stress is much smaller than the localised lattice distortion caused by dislocation accumulation.

5 Conclusions

SKPFM can be a useful tool for characterizing the gradient strengthened layer induced by USRP. A correlation between dislocation density, the SKPFM measured Volta potential and the residual stress was demonstrated experimentally in the gradient layer of 20CrMnTi steel, that is, in the plastic deformation region, Volta potential increased due to the dislocation density increase, while in the elastic deformation zone, the residual tensile stress leads to a slight increase in the Volta potential. In addition, due to the dislocation pile-up, there is a local Volta potential fluctuation in the plastic

deformation region, while in the elastic deformation region, the potential map is very flat without fluctuations.

Captions of Figures

Fig.1. Schematic diagram of the experimental setting.

Fig.2. Polarization curves of 20CrMnTi in solution with pH=8.45 and $\text{Cl}^- = 0.05\text{mol/L}$ under different rolling pressures.

Fig.3. Statistical results of the variation of the passivation current and passivation range with the rolling pressure.

Fig.4. EBSD surface grains map of 20CrMnTi under different rolling pressures: a) 0.1 MPa; b) 0.15 MPa; c) 0.20 MPa.

Fig.5. The average grain size and fraction of fine grains (mean diameter less than $2\ \mu\text{m}$) of different specimens.

Fig.6. (left) TEM micrographs of typical lath martensite and (right) High-resolution TEM images; the inset is the Fourier -reconstructed image showing dislocations (circled in red). (a-b) untreated; (c-d) 0.1 MPa; (e-f) 0.15 MPa; (g-h) 0.2 MPa.

Fig.7. Dislocation density values of different specimens.

Fig.8. The morphologies of 0.2MPa after argon ion polishing: (a) SEM micrograph and (c) AFM topography in the strengthened layer; (b) SEM micrograph and (d) AFM topography in the matrix.

Fig.9. Topography and Volta potential maps of 0.2 MPa at different depths from the

surface: (a) 45 μm ; (b)100 μm and (c) 800 μm .

Fig.10. Topography and Volta potential maps of 0.15 MPa at different depth from the surface, (a) 27 μm ; (b) 130 μm and (c) 700 μm .

Fig.11. Topography and Volta potential maps of 0.1MPa at different depths from the surface, (a) 51 μm ; (b) 115 μm and (c) 600 μm .

Fig.12. In-depth axial residual stress and Volta potential distributions in different specimens, (a) 0.1 MPa; (b) 0.15 MPa; (c) 0.2 MPa.

Fig.13. SEM microstructure of the rolled samples at different depths from the surface, (a) and (d) 0.1 Mpa; (b) and (e) 0.15 Mpa; (c) and (f) 0.2 Mpa; (a-c) 0-100 μm ; (d-f) 200-300 μm .

Fig.14. Diagram of the relationship between Volta potential and dislocation density at grain boundaries.

Fig.15. Topography and Volta potential linear profiles of 0.2MPa marked by the red line in Fig.9a.

Fig.16. Schematic diagram of the change in Volta potential in the strengthened layer.

Acknowledgements

This work was supported by the National Natural Science Foundation of China [grant numbers 51801038, 51774103, 51661006]; The Program of “One Hundred Talented People” of Guizhou Province [grant number 20164014]; Guizhou Province

Science and Technology Project [grant numbers 20175656, 20175788, 20185781, 20191414]; and The Program for Innovative Research Team of Guizhou Province Education Ministry.

Author contributions

Tao Cheng performed measurements and writing- Original draft preparation

Wei Shi: conception, experimental design, funding acquisition

Song Xiang: funding acquisition, resources

Ronald G. Ballinger: editing

Conflicts of interest

The authors declared that they have no conflicts of interest to this work.

We declare that we do not have any commercial or associative interest that represents a conflict of interest in connection with the work submitted.

Reference

- [1]W Ting, W Dongpo, L Gang, G Baoming, S Ningxia (2008) Investigations on the nanocrystallization of 40Cr using ultrasonic surface rolling processing, *Applied Surface Science* 255: 1824.
- [2]LX Lu, J Sun, L Li, QC Xiong (2016) Study on surface characteristics of 7050-T7451 aluminum alloy by ultrasonic surface rolling process, *International Journal of Advanced Manufacturing Technology* 87: 1.
- [3]M Abdulstaar, M Mhaede, M Wollmann, L Wagner (2014) Investigating the effects of bulk and surface severe plastic deformation on the fatigue, corrosion behaviour and corrosion fatigue of AA5083, *Surface and Coatings Technology* 254: 244.
- [4]T Balusamy, S Kumar, TSN Sankara Narayanan (2010) Effect of surface nanocrystallization on the corrosion behaviour of AISI 409 stainless steel, *Corrosion Science* 52: 3826.
- [5]S Jelliti, C Richard, D Retraint, T Roland, M Chemkhi, C Demangel (2013) Effect of surface

nanocrystallization on the corrosion behavior of Ti-6Al-4V titanium alloy, *Surface and Coatings Technology* 224: 82.

[6]N Li, S Shi, J Luo, J Lu, N Wang (2017) Effects of surface nanocrystallization on the corrosion behaviors of 316L and alloy 690, *Surface and Coatings Technology* 309: 227.

[7]Y Lin, J Lu, L Wang, T Xu, Q Xue (2006) Surface nanocrystallization by surface mechanical attrition treatment and its effect on structure and properties of plasma nitrided AISI 321 stainless steel, *Acta Materialia* 54: 5599.

[8]Q Sun, Q Han, R Xu, K Zhao, J Li (2018) Localized corrosion behaviour of AA7150 after ultrasonic shot peening: Corrosion depth vs. impact energy, *Corrosion Science* 130: 218.

[9]Z Ye, D Liu, C Li, X Zhang, Z Yang, M Lei (2014) Effect of Shot Peening and Plasma Electrolytic Oxidation on the Intergranular Corrosion Behavior of 7A85 Aluminum Alloy, *Acta Metallurgica Sinica (English Letters)* 27: 705.

[10]S Doja, L Bichler, S Fan (2017) Corrosion Behavior of AZ31 Magnesium Alloy in Highly Alkaline Environment, *Acta Metallurgica Sinica (English Letters)* 30: 367.

[11]AQ Lü, Y Zhang, Y Li, G Liu, QH Zang, CM Liu EFFECT OF NANOCRYSTALLINE AND TWIN BOUNDARIES ON CORROSION BEHAVIOR OF 316L STAINLESS STEEL USING SMAT, *Acta Metallurgica Sinica(English Letters)* 19: 0.

[12]P Chui, K Sun, C Sun, X Yang, T Shan (2011) Effect of surface nanocrystallization induced by fast multiple rotation rolling on hardness and corrosion behavior of 316L stainless steel, *Applied Surface Science* 257: 6787.

[13]TG S. Sadewasser (2012) *Kelvin Probe Force Microscopy Measuring and Compensating Microscopy*, Springer, Heidelberg.

[14]M Nonnenmacher, MP O'Boyle, HK Wickramasinghe (1991) Kelvin probe force microscopy, *Applied Physics Letters* 58: 2921.

[15]TdS Corey M. Efav (2019) *Toward Improving Ambient Volta Potential Measurements with SKPFM for Corrosion Studies*, The Electrochemical Society.

[16]C Örneke, DL Engelberg (2015) SKPFM measured Volta potential correlated with strain localisation in microstructure to understand corrosion susceptibility of cold-rolled grade 2205 duplex stainless steel, *Corrosion Science* 99: 164.

[17]E Rahimi, A Rafsanjani-Abbasi, A Imani, S Hosseinpour, A Davoodi (2018) Correlation of surface Volta potential with galvanic corrosion initiation sites in solid-state welded Ti-Cu bimetal using AFM-SKPFM, *Corrosion Science* 140: 30.

[18]A Ma, L Zhang, D Engelberg, Q Hu, S Guan, Y Zheng (2019) Understanding crystallographic orientation dependent dissolution rates of 90Cu-10Ni alloy: New insights based on AFM/SKPFM measurements and coordination number/electronic structure calculations, *Corrosion Science*: 108320.

[19]C Örneke, C Leygraf, J Pan (2019) On the Volta potential measured by SKPFM – fundamental and practical aspects with relevance to corrosion science, *Corrosion Engineering, Science and Technology* 54: 185.

[20]W Li, Y Wang, DY Li (2004) Response of the electron work function to deformation and yielding

behavior of copper under different stress states, *physica status solidi (a)* 201: 2005.

[21]WLaDY LI (2003) EFFECT OF GRAIN SIZE ON THE ELECTRON WORK FUNCTION OF Cu AND Al.

[22]W Li, DY Li (2005) Effect of surface geometrical configurations induced by microcracks on the electron work function, *Acta Materialia* 53: 3871.

[23]F Robin, H Jacobs, O Homan, A Stemmer, W Bachtold (2000) Investigation of the cleaved surface of a p-i-n laser using Kelvin probe force microscopy and two-dimensional physics simulations, *Applied Physics Letters* 76: 2907.

[24]AB Cook, Z Barrett, SB Lyon, HN McMurray, J Walton, G Williams (2004) Calibration of the scanning Kelvin probe force microscope under controlled environmental conditions, *Electrochimica Acta* 49: 100.

[25]M Rohwerder, F Turcu (2007) High-resolution Kelvin probe microscopy in corrosion science: Scanning Kelvin probe force microscopy (SKPFM) versus classical scanning Kelvin probe (SKP), *Electrochimica Acta* 53: 290.

[26]C Örnek, C Leygraf, J Pan (2019) Passive film characterisation of duplex stainless steel using scanning Kelvin probe force microscopy in combination with electrochemical measurements, *npj Materials Degradation* 3.

[27]VV Levitin, SV Loskutov, MI Pravda, BA Serpetzky (1994) Influence of cyclic stresses upon the electronic work function for the metal surface, *Solid State Communications* 92: 973.

[28]W Li, DY Li (2013) Effects of dislocation on electron work function of metal surface, *Materials Science and Technology* 18: 1057.

[29]J Guo, H Fu, B Pan, R Kang (2019) Recent progress of residual stress measurement methods: A review, *Chinese Journal of Aeronautics*.

[30]HR Huang, XY Li (2012) The Deduction and Application of Correction Formulas of Three-Dimensional Residual Stress with Layer Stripping Method, *Advanced Materials Research* 476-478: 2608.

Captions of Figures

Fig.1. Schematic diagram of the experimental setting.

Fig.2. Polarization curves of 20CrMnTi in solution with pH=8.45 and $Cl^- = 0.05\text{mol/L}$ under different rolling pressures.

Fig.3. Statistical results of the variation of the passivation current and passivation range with the

rolling pressure.

Fig.4. EBSD surface grains map of 20CrMnTi under different rolling pressures: a) 0.1 MPa; b) 0.15 MPa; c) 0.20 MPa.

Fig.5. The average grain size and fraction of fine grains (mean diameter less than 2 μm) of different specimens.

Fig.6. (left) TEM micrographs of typical lath martensite and (right) High-resolution TEM images; the inset is the Fourier -reconstructed image showing dislocations (circled in red). (a-b) untreated; (c-d) 0.1 MPa; (e-f) 0.15 MPa; (g-h) 0.2 MPa.

Fig.7. Dislocation density values of different specimens.

Fig.8. The morphologies of 0.2MPa after argon ion polishing: (a) SEM micrograph and (c) AFM topography in the strengthened layer; (b) SEM micrograph and (d) AFM topography in the matrix

Fig.9. Topography and Volta potential maps of 0.2 MPa at different depths from the surface: (a) 45 μm ; (b)100 μm and (c) 800 μm .

Fig.10. Topography and Volta potential maps of 0.15 MPa at different depth from the surface, (a) 27 μm ; (b) 130 μm and (c) 700 μm .

Fig.11. Topography and Volta potential maps of 0.1MPa at different depths from the surface, (a) 51 μm ; (b) 115 μm and (c) 600 μm .

Fig.12. In-depth axial residual stress and Volta potential distributions in different specimens, (a) 0.1 MPa; (b) 0.15 MPa; (c) 0.2 MPa.

Fig.13. SEM microstructure of the rolled samples at different depths from the surface, (a) and (d) 0.1 MPa; (b) and (e) 0.15 MPa; (c) and (f) 0.2 MPa; (a-c) 0-100 μm ; (d-f) 200-300 μm .

Fig.14. Diagram of the relationship between Volta potential and dislocation density at grain boundaries.

Fig.15. Topography and Volta potential linear profiles of 0.2MPa marked by the red line in Fig.9a.

Fig.16. Schematic diagram of the change in Volta potential in the strengthened layer.

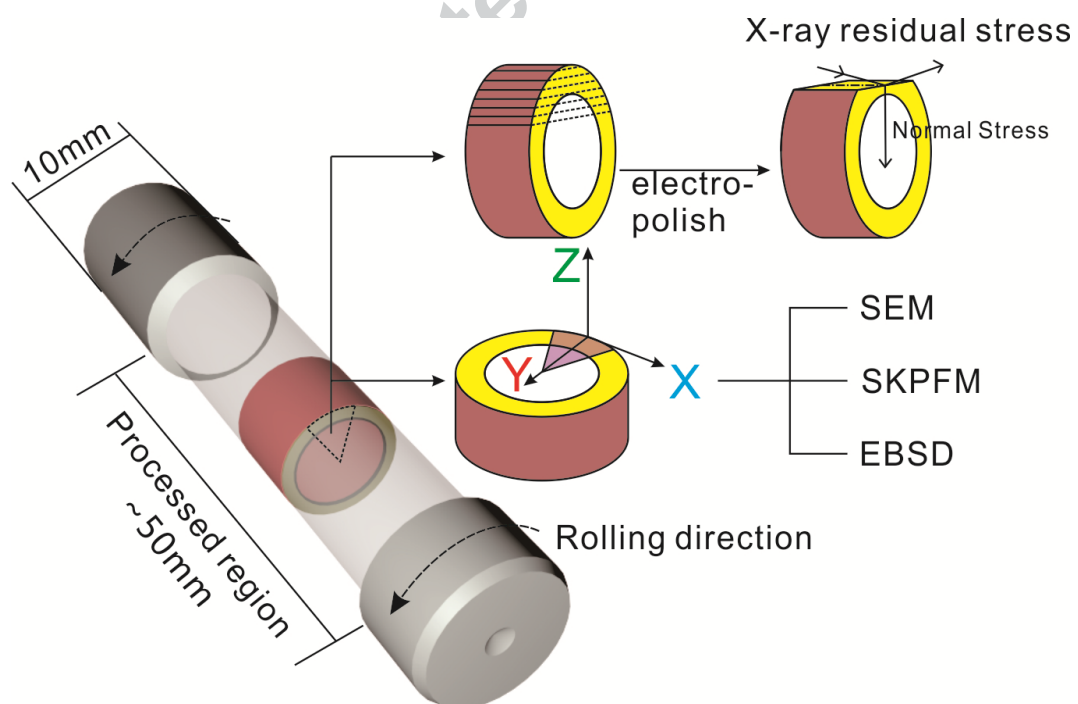


Fig.1 Schematic diagram of the experimental setting

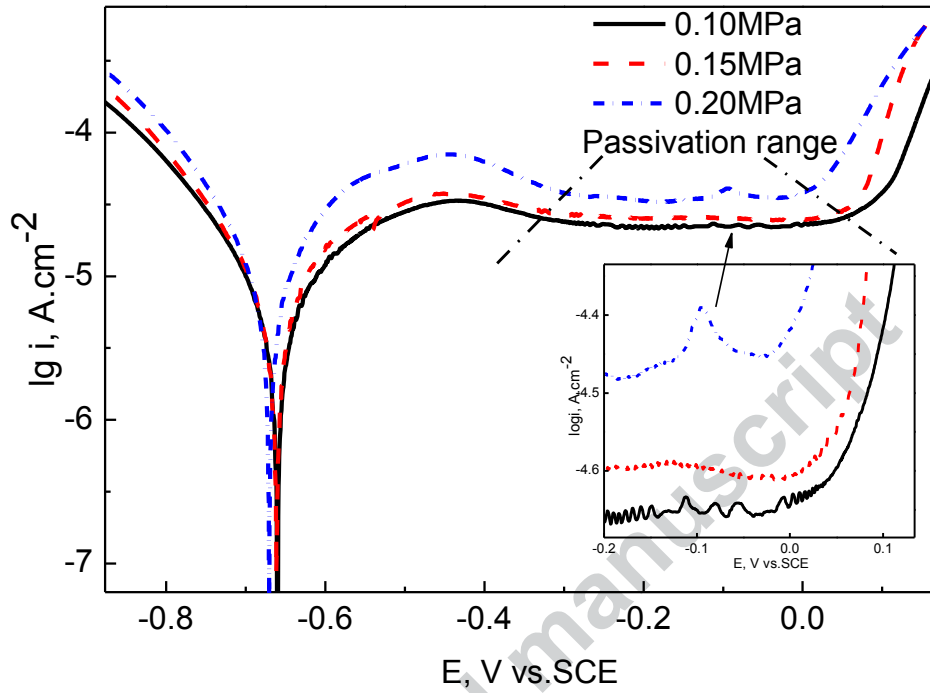


Fig.2 Polarization curves of 20CrMnTi in solution with pH=8.45 and Cl⁻=0.05 mol/L under different rolling pressures.

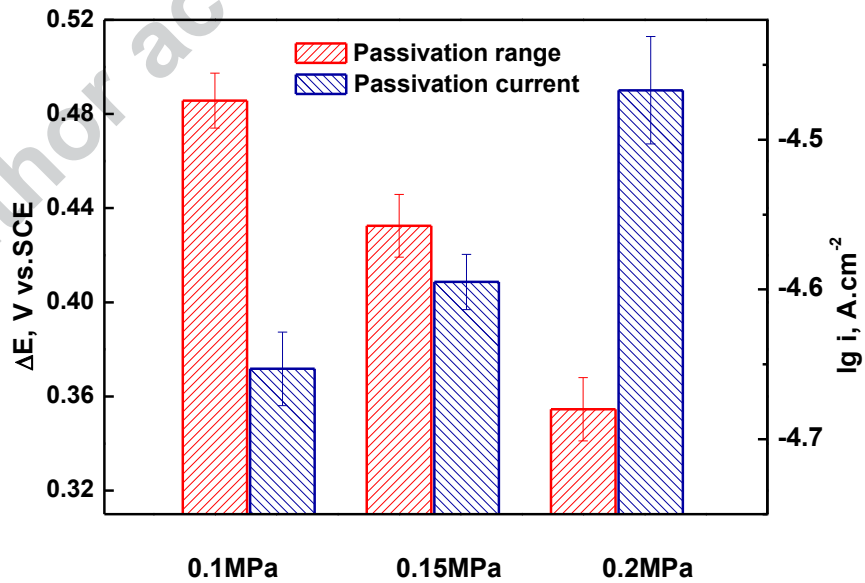


Fig.3. Statistical results of the variation of the passivation current and passivation range with the

rolling pressure.

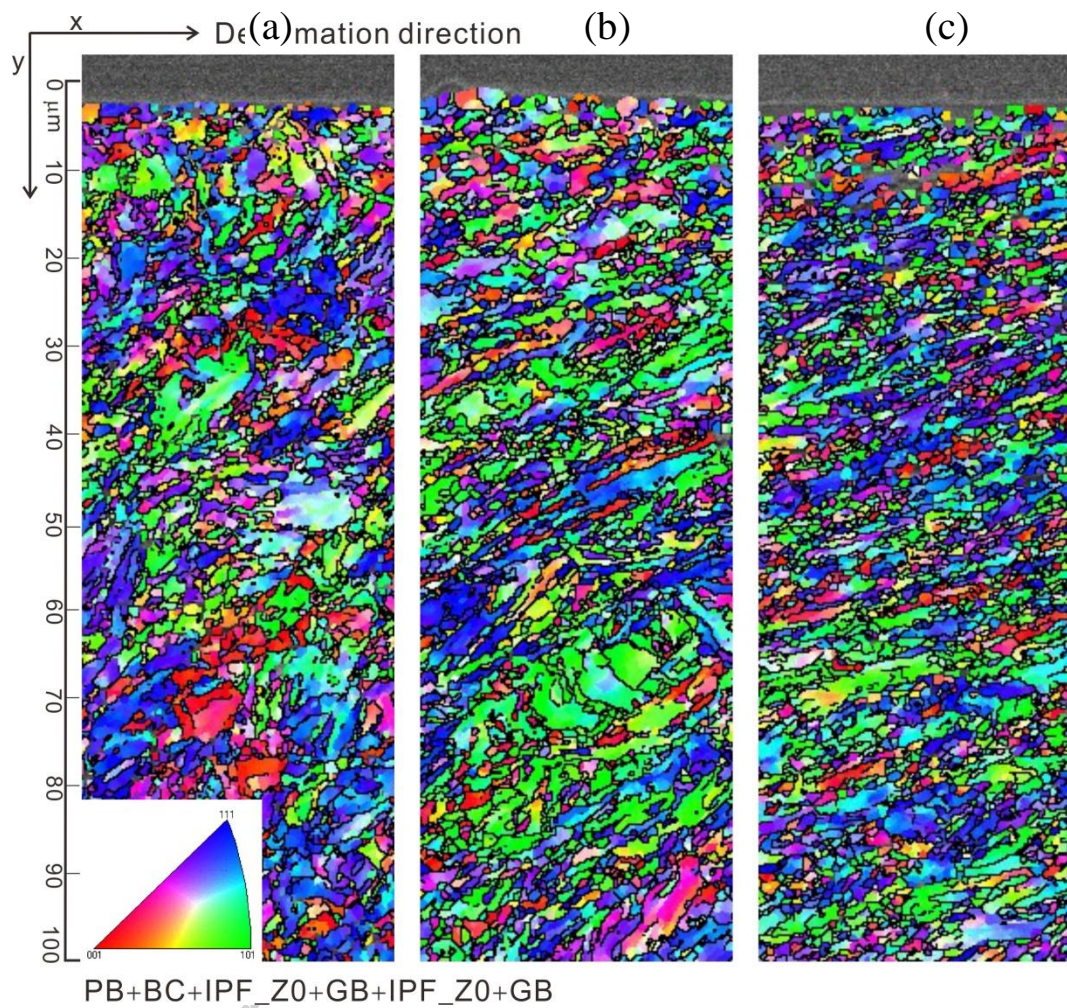


Fig.4. EBSD surface grains map of 20CrMnTi under different rolling pressures: a) 0.1 Mpa; b) 0.15 Mpa; c) 0.20 Mpa.

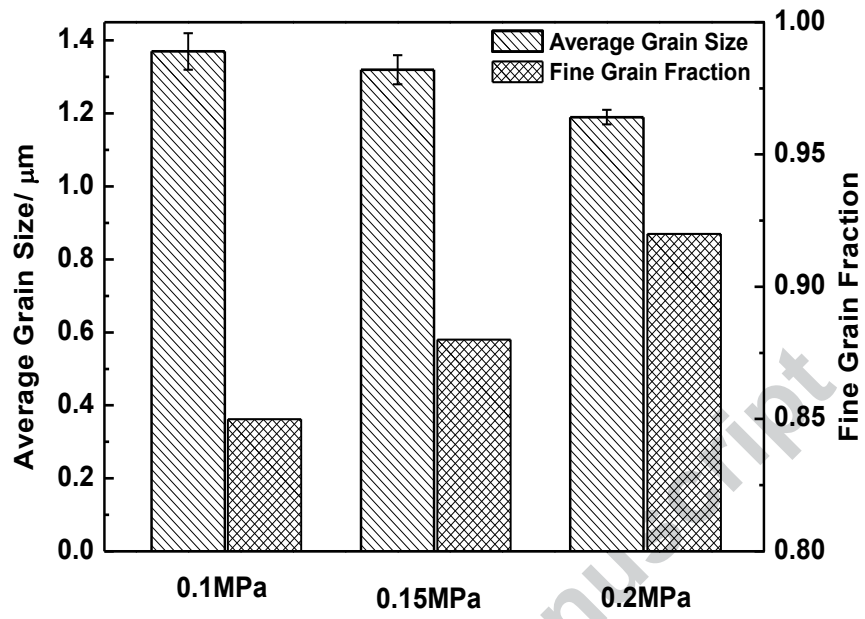
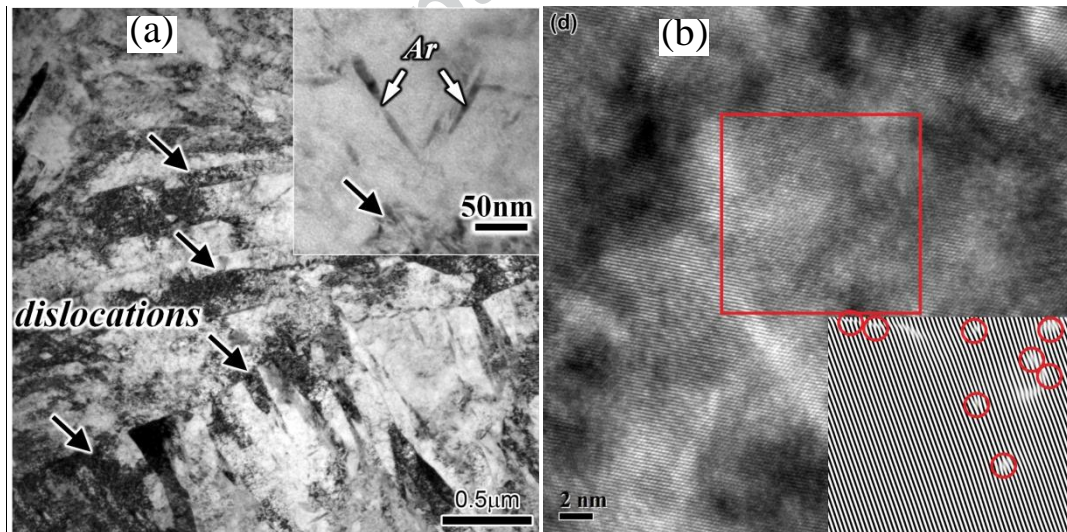


Fig.5. The average grain size and fraction of fine grains (mean diameter less than 2 μm) of different specimens.



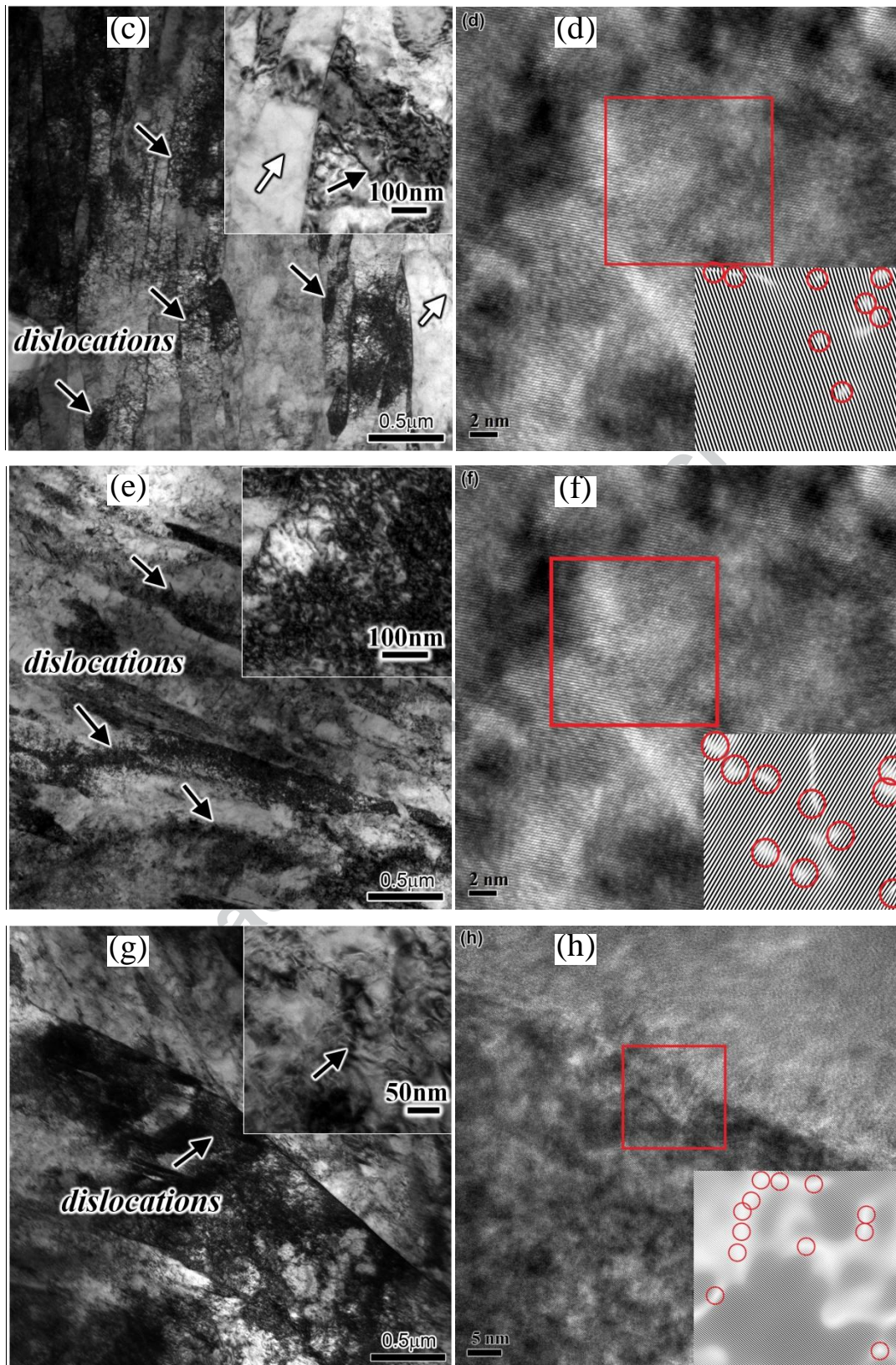


Fig.6. (left) TEM micrographs of typical lath martensite and (right) High-resolution TEM

images; the inset is the Fourier-reconstructed image showing dislocations (circled in red). (a-b)

untreated; (c-d) 0.1 MPa; (e-f) 0.15 MPa;

(g-h) 0.2 MPa.

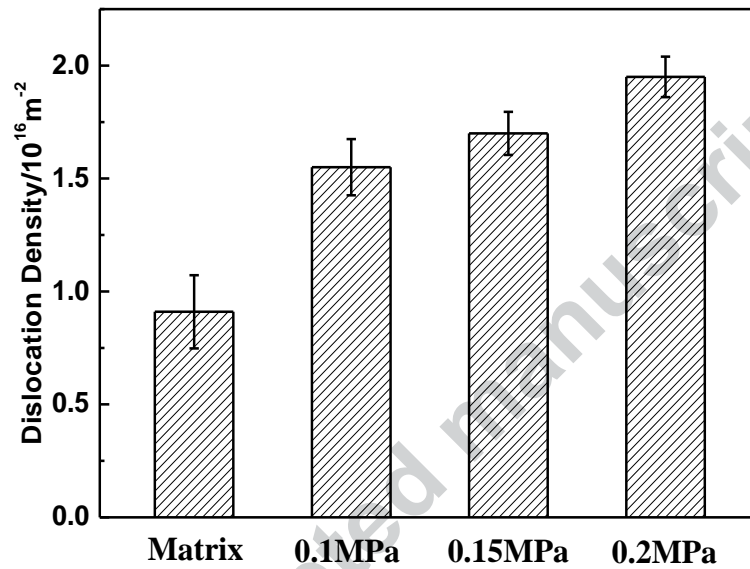
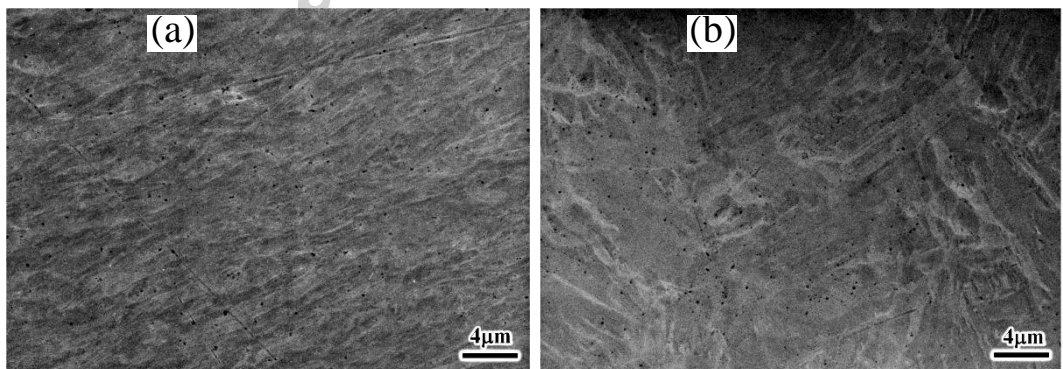


Fig.7. Dislocation density values of different specimens.



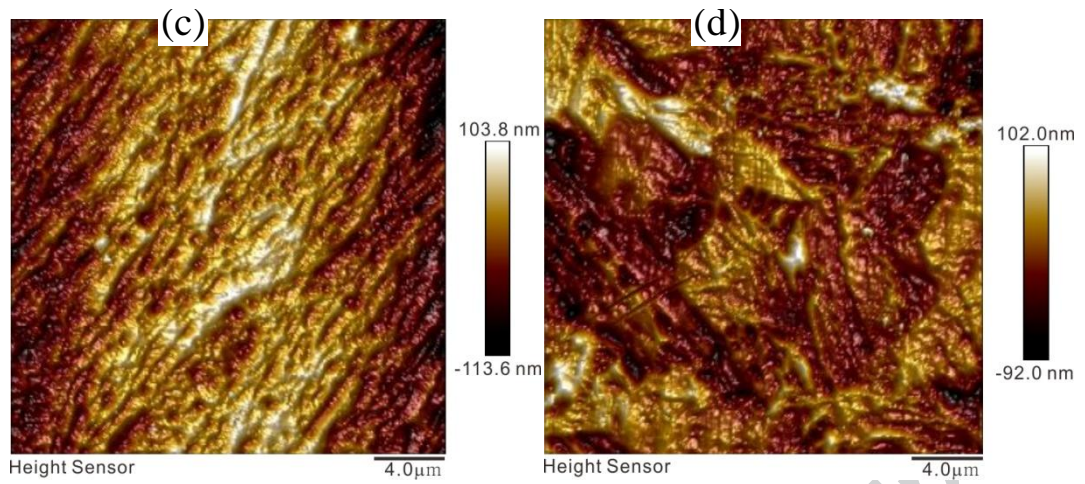
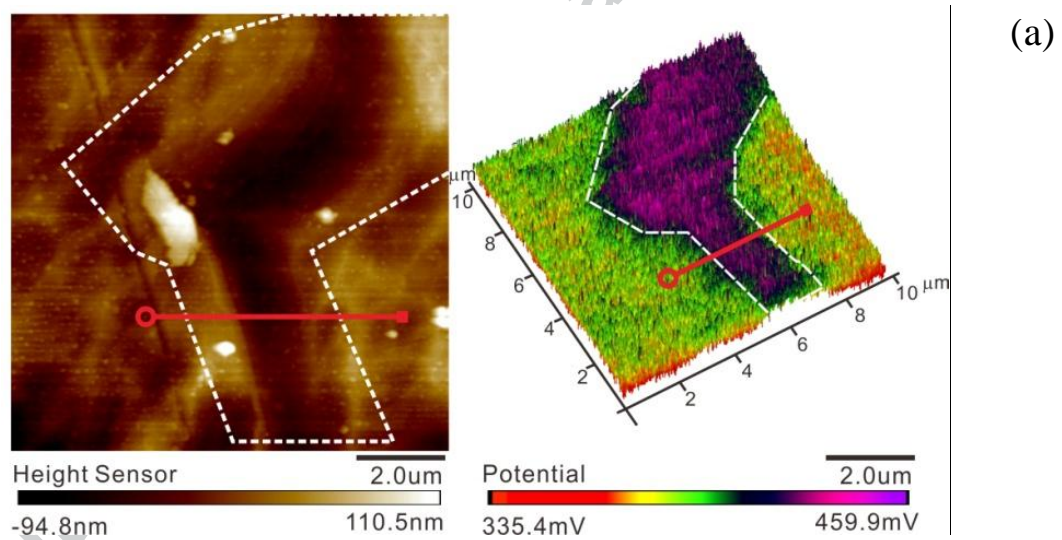


Fig.8. The morphologies of 0.2MPa after argon ion polishing: (a) SEM micrograph and (c) AFM topography in the strengthened layer; (b) SEM micrograph and (d) AFM topography in the matrix



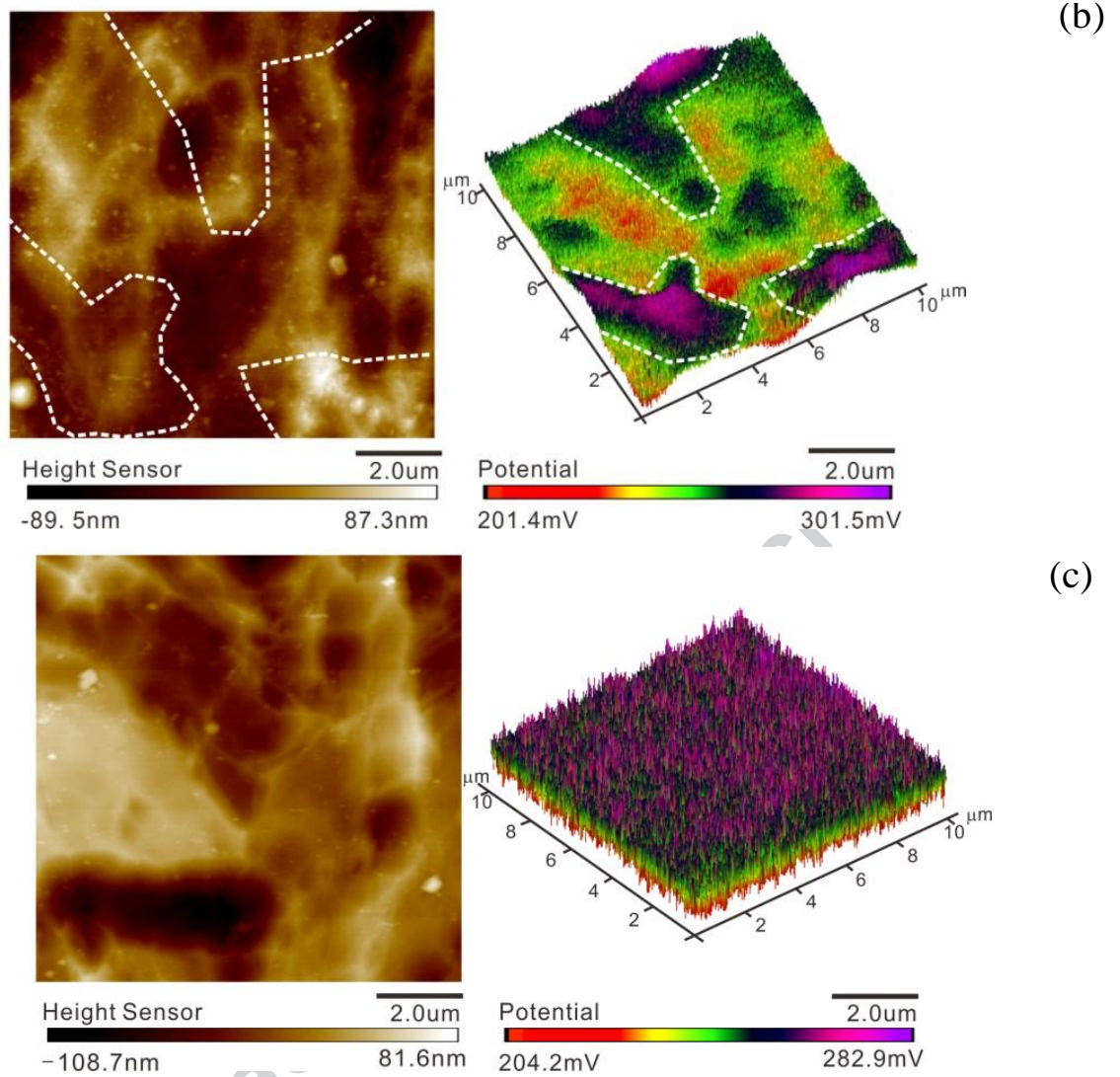


Fig.9. Topography and Volta potential maps of 0.2 MPa at different depths from the surface: (a) 45 μm ; (b) 100 μm and (c) 800 μm .

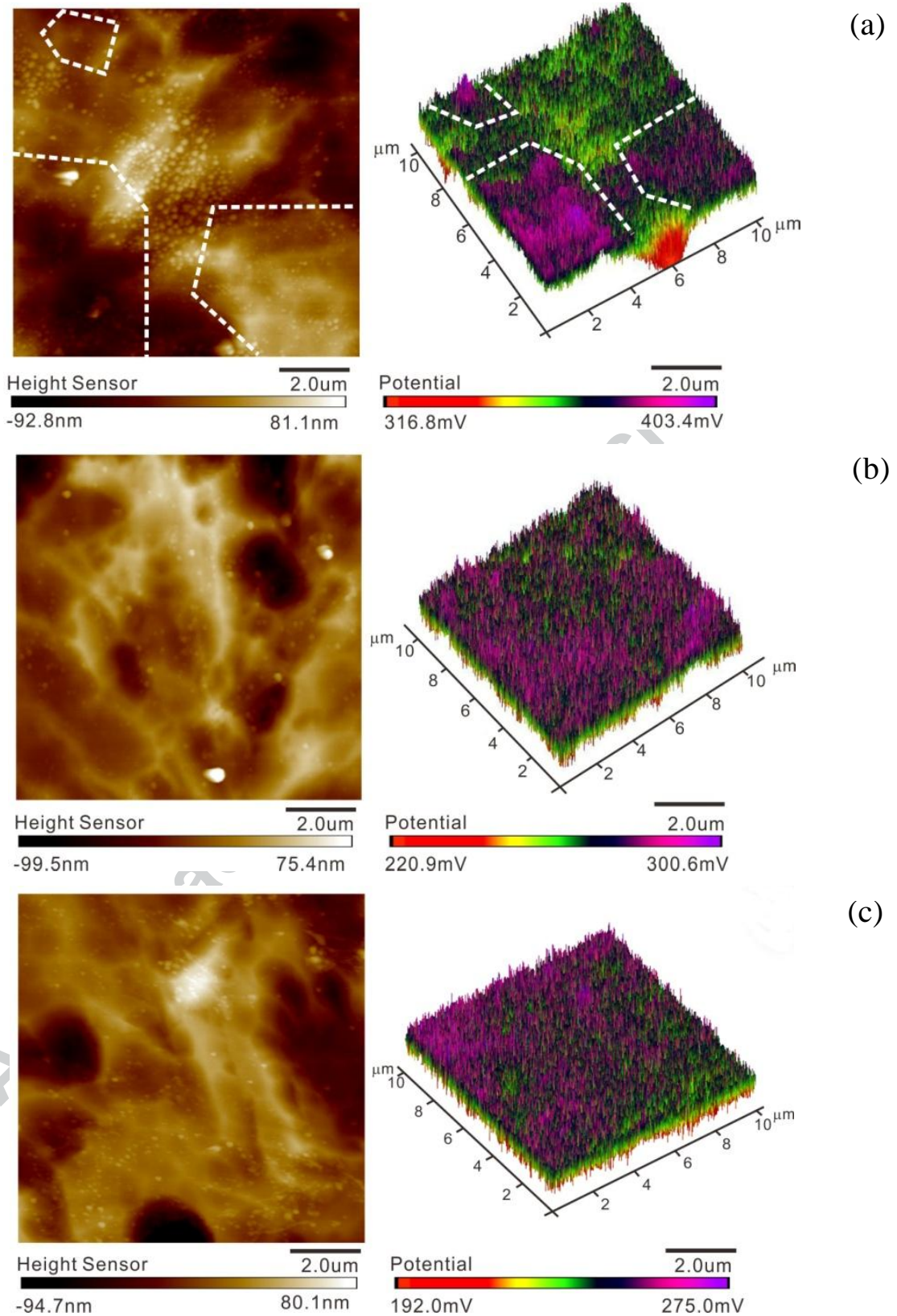


Fig.10. Topography and Volta potential maps of 0.15 MPa at different depths from the surface,

(a) 27 μm ; (b) 130 μm and (c) 700 μm .

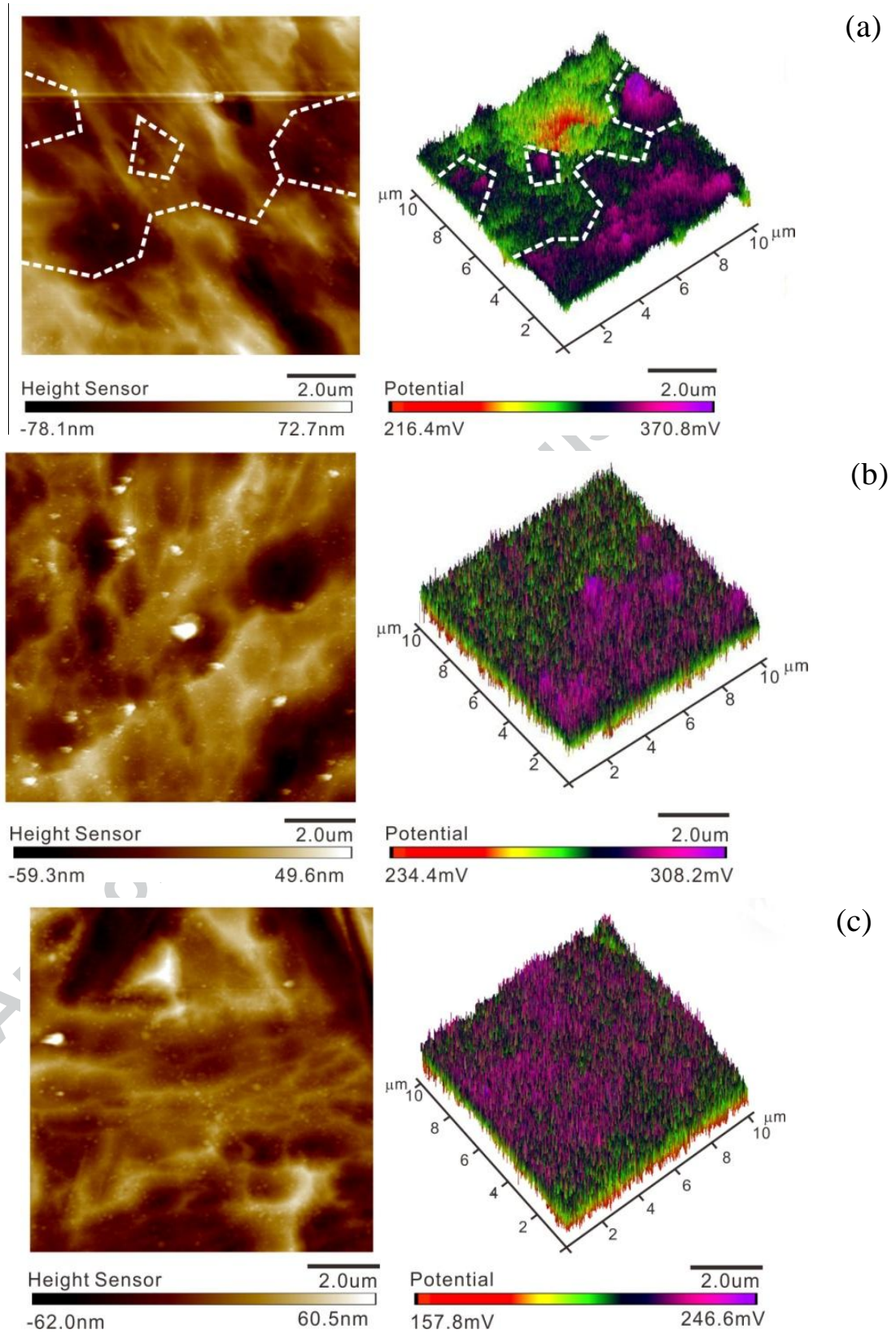
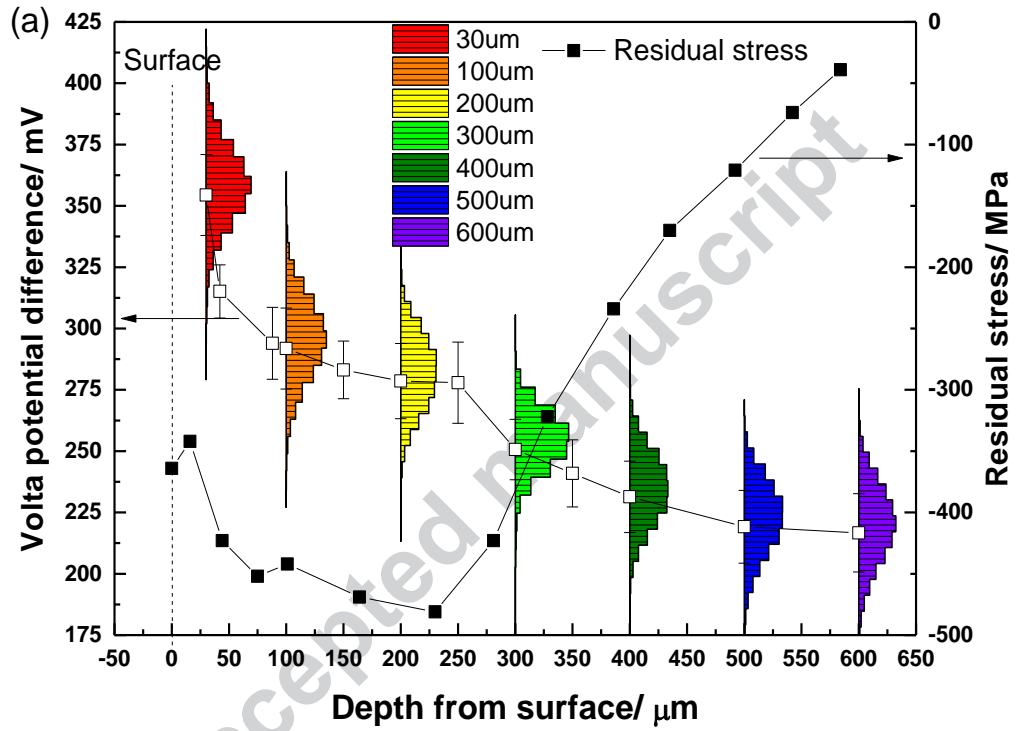


Fig.11. Topography and Volta potential maps of 0.1 MPa at different depths from the surface, (a) 51 μm ; (b) 115 μm and (c) 600 μm .



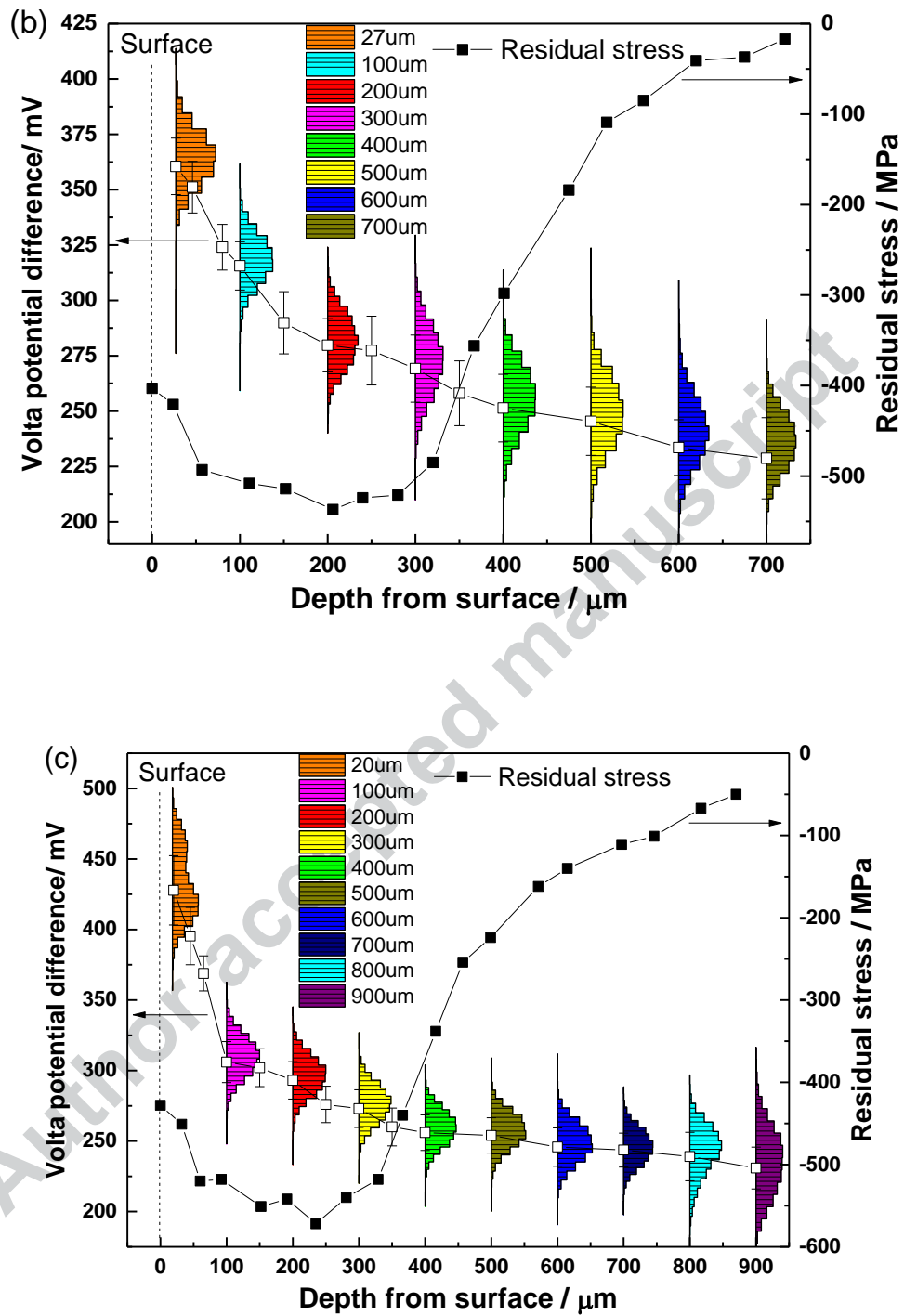
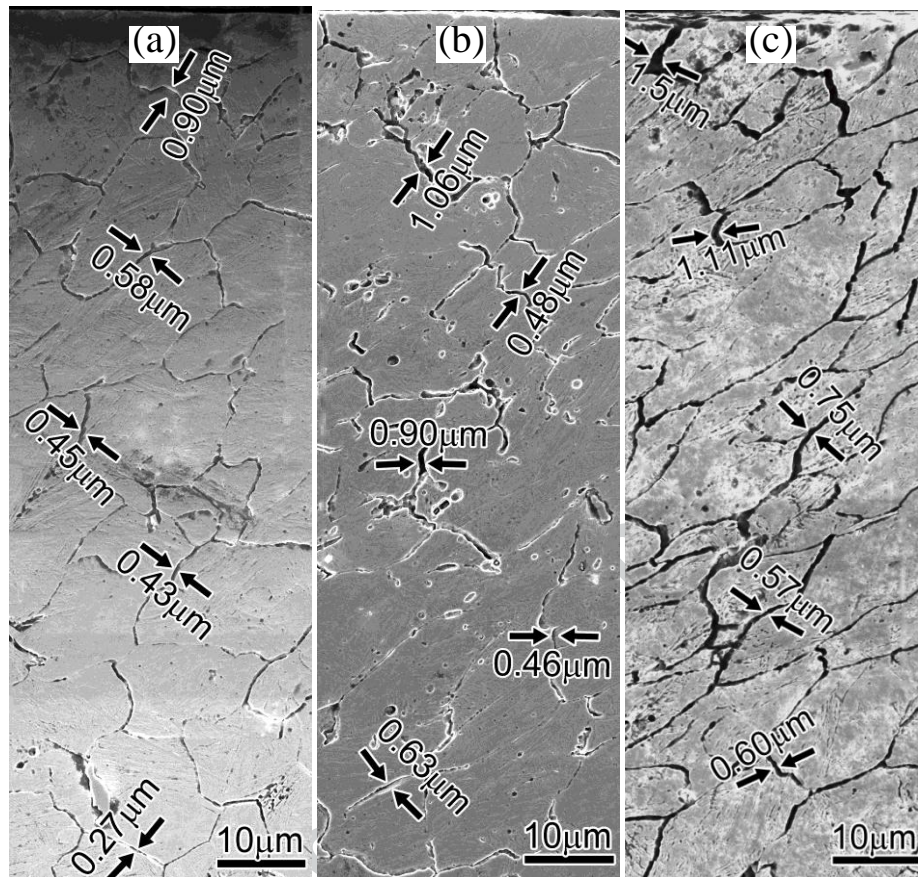


Fig.12. In-depth axial residual stress and Volta potential distributions in different specimens, (a)

0.1 MPa; (b) 0.15 MPa;

(c) 0.2 MPa.



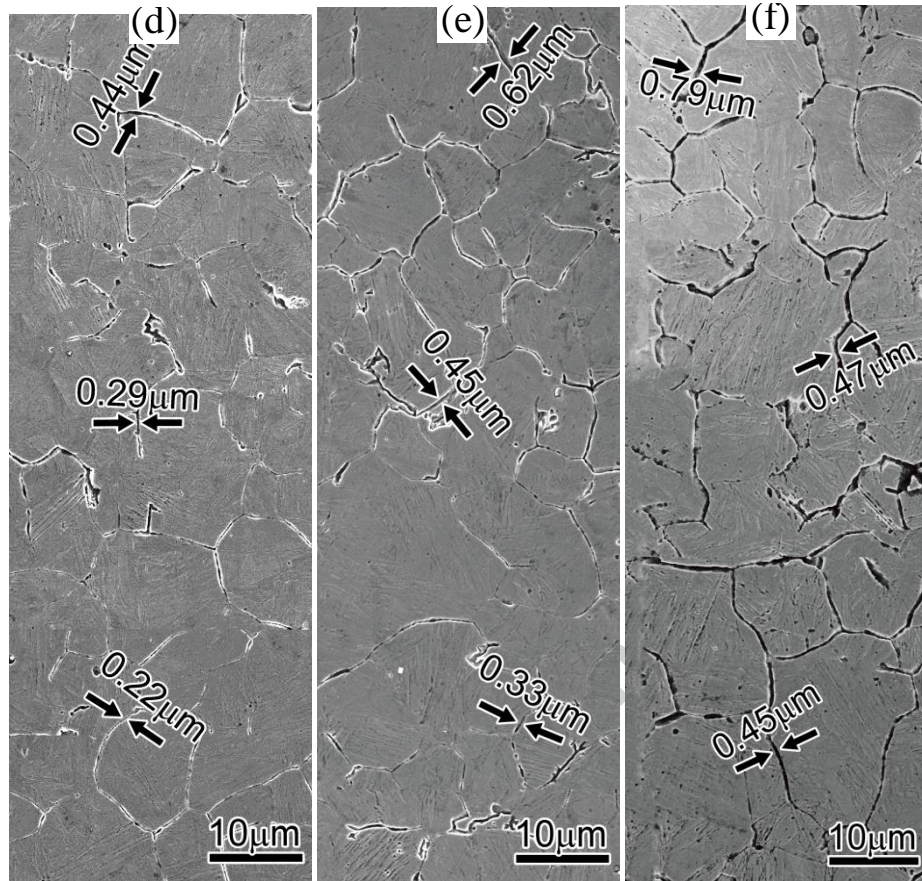


Fig.13. SEM microstructure of the rolled samples at different depths from the surface, (a) and (d) 0.1 Mpa; (b) and (e) 0.15 Mpa; (c) and (f) 0.2 Mpa; (a-c) 0-100 μm; (d-f) 200-300 μm.

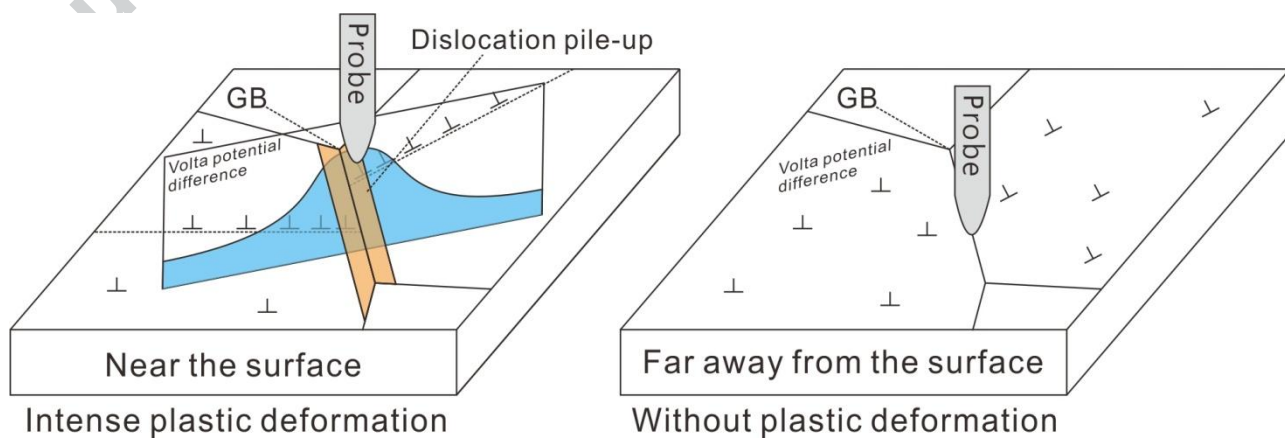


Fig.14 Diagram of the relationship between Volta potential and dislocation density at grain boundaries

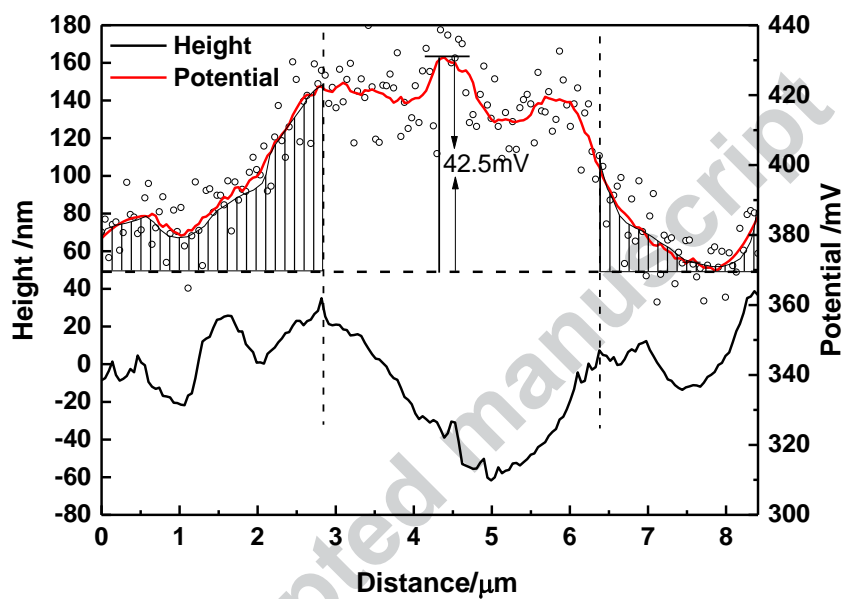


Fig.15. Topography and Volta potential linear profiles of 0.2 MPa marked by the red line in Fig.

9a.

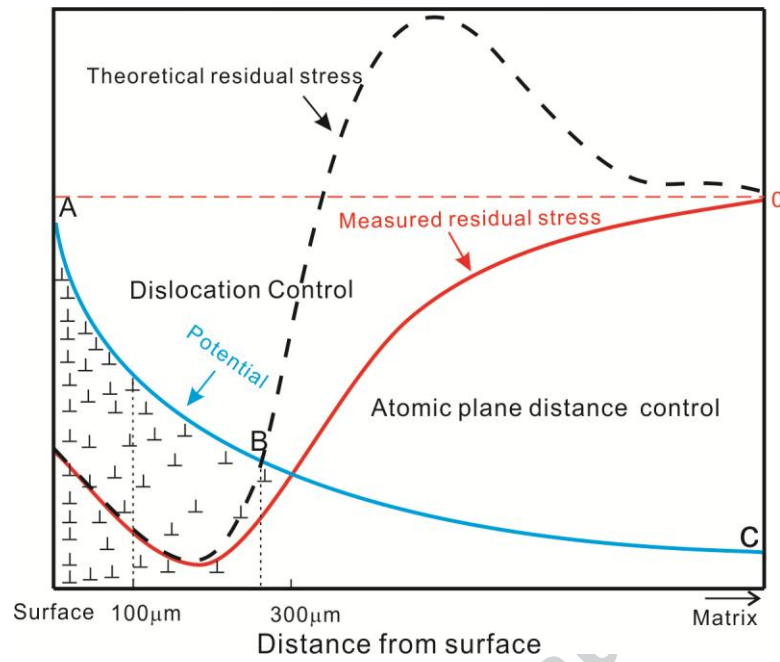


Fig.16. Schematic diagram of the change in Volta potential in the strengthened layer.